Molecular Aggregation State and Photovoltaic Properties of Chlorophyll-Doped Conducting Poly(3-hexylthiophene)/MCM-41 Nanocomposites

Weng On Yah,[§] Zhe Wang,[†] Hideyuki Otsuka,[§,†] Kenichi Kato,[‡,||] Jungeun Kim,[†] Masaki Takata,[‡,||] and Atsushi Takahara*,[§,†]

Graduate School of Engineering and Institute of Materials Chemistry and Engineering, Kyushu University, 744 Motooka, Nishi-ku, Fukuoka 819-0395, Japan, Japan Synchrotron Radiation Research Institute, 1-1-1 Kouto, Sayo-cho, Sayo-gun, Hyogo 679-5148, Japan, and RIKEN SPring-8 Center, 1-1-1 Kouto, Sayo-cho, Sayo-gun, Hyogo 679-5148, Japan

ABSTRACT Chlorophyll (Chl) was immobilized into a 1,4-butanediol-modified MCM-41 (BMCM-41) intercalated by poly(3-hexylthiophene) (P3HT) to form BMCM-41/P3HT/Chl nanocomposites having P3HT contents of 10, 30, 60, and 90 wt % from a solution-casting method. Wide-angle X-ray diffraction and transmission electron microscopy studies indicate that the pore structure of MCM-41 was retained after surface modification and a subsequent P3HT intercalation process. Scanning electron microscopy images showed that the BMCM-41 nanoparticles dispersed into the polymer matrix of BMCM-41/P3HT/Chl, and the sample with 10 wt % P3HT content gives the most homogeneous nanoparticle dispersion. Nitrogen adsorption–desorption results confirmed that the P3HT intercalation and Chl immobilization inside the BMCM-41 mesopore were successfully carried out. The pore volume and surface area of BMCM-41 decreased significantly when the amount of P3HT was increased from 10 to 90 wt %. The UV–vis study showed a blue shift of the π–π* transition band of P3HT in the spectra of BMCM-41/P3HT/Chl nanocomposites. The FT-IR study indicates an increase of the thiophene ring stretching and a decrease of the C=O stretching when P3HT and Chl were inside the mesopore. The photovoltaic property of Chl-doped P3HT was improved significantly upon the addition of BMCM-41 nanoparticles, and BMCM-41/P3HT-10/Chl exhibits the highest incident photon-to-current conversion efficiency of 7.16%.

KEYWORDS: MCM-41 • poly(3-hexylthiophene) • chlorophyll • photovoltaic devices • nanocomposite • dye immobilization • polymer intercalation

1. INTRODUCTION

In the modern development of plastic electronics, molecular doping of semiconducting polymers is a critical process to enhancing the device performance. Recent studies have demonstrated that polymer functions, e.g., light absorption, luminescence, or electronic conductivity, could be improved by doping with dye (1−4). Since then, these dye-doped polymers with novel properties have been applied in diverse plastic electronics such as photovoltaic cells (5), photoconductors (6), photorefractive materials (7), and junction devices (8). As for photovoltaic cells, the introduction of dopants into the conjugated system of semiconducting polymers provides additional free charge carriers that result in higher conductivity. Additionally, doping of semiconducting polymers has been used to broaden the spectral response of devices (9).

The use of polymers for conversion of solar energy is economically advantageous because of their light weight, low cost, and mechanical flexibility. One of the most studied conducting polymers is poly(3-hexylthiophene) (P3HT) because of its excellent conductivity and solution processability, which increase its potential commercial importance (10). P3HT is an efficient electron-donor material, and when in regioregular form, it exhibits a high degree of intermolecular ordering, leading to high charge carrier mobility. The conductivity of P3HT could be further increased when electrons are added or removed from conjugated π orbitals via doping. Murata et al. reported an enhanced photocurrent of P3HT by blending with monomeric porphyrins of different oxidation potentials (11). Later, they extended their research by examining the effect of adding a TiO₂ electrode in a blended solid of P3HT and merocyanine (12). However, the efficiency of this device still did not reach the satisfaction level for practical use. On the other hand, Krebs and Biancardo studied a photovoltaic cell consisting of P3HT covalently linked to a zwitterionic ruthenium dye that can bind to TiO₂ (13). The cell showed good stability even after 30 h of

illumination with effective light harvesting and energy transfer from P3HT to the ruthenium dye.

From the perspective of fabricating an artificial photosynthetic system, a photosynthetic dye like chlorophyll (Chl) that absorbs visible light ranging from 400 to 700 nm is essential for solar energy conversion. This natural dye, found in chloroplast of green plants, consists of a porphyrin ring that coordinates to a central magnesium ion (14). The semiconducting properties in Chl are mainly due to electron delocalization around the porphyrin's conjugation system. Chl is able to work as both an electron donor and an electron acceptor in charge-transfer complexes by donating (n-doping) and accepting (p-doping) electrons, respectively (15). These distinctive characteristics can offer some promising applications in the field of organic electronic devices. For example, Araki et al. prepared the Chl/(water-soluble polymer) complex of poly(vinyl alcohol) (PVA) as an artificial model system for a natural Chl—protein complex (16). The magnesium ion and conjugated system of Chl significantly improved the PVA conductivity and dielectric constants, turning it into an attractive material for polymeric capacitors (17). However, this natural dye cannot be directly used in an organic solvent because of its instability and inactivation. In order to obtain a homogeneous system with good stability, Chl should be chemically modified (18) or immobilized into an inorganic support (19). The fixation of Chl into an inorganic material provides a synergic effect of the high selective activity of a dye and the chemical and mechanical stability of an inorganic support. Inada et al. have reported that Chl conjugated with montmorillonite was found to be photostable compared to that in a benzene solution (19), which demonstrated the importance of Chl—support interactions. In order to collect sunlight efficiently, a large amount of Chl needs to be arranged in a certain pattern for efficient energy transfer. Thus, the high surface area and high thermal stability of MCM-41 (20) is employed to encapsulate Chl inside its pore. MCM-41 is a family of silicate mesoporous molecular sieves and has hexagonally packed arrays of one-dimensional channels with much larger surface area and narrower pore-size distribution than ordinary amorphous silica. The mesoporous MCM-41 is expected to act as a filler in nanocomposites and can influence the arrangement of P3HT chains because it may become confined in a MCM-41 nanoscale pore (21).

In this paper, Chl-doped P3HT/MCM-41 having different polymer weight percents is prepared through a solution-casting method. The effect of the polymer content on the physical and photovoltaic properties of nanocomposites is presented. A more constricted characterization can determine how the photoconductivity of conjugated P3HT is affected by chain intercalation in the mesopore of MCM-41. The unique enhancement of the photocurrent properties of these nanocomposites by blending with MCM-41 is also discussed.

2. EXPERIMENTAL SECTION

2.1. Materials. Chlorophyll a was purchased from Wako Pure Chemical Industries, Ltd. Regioregular poly(3-hexylthiophene) (P3HT; average molecular weight of ca. 64 000) and indium—tin oxide (ITO)-coated glass substrates ($8-12 \ \Omega \ sq^{-1}$) were obtained from Aldrich Chemicals. Organic light-emitting device grade poly(3,4-ethylenedioxythiophene)—poly(styrenesulfonate) (PEDOT—PSS) was purchased from Polysciences, Inc. All chemicals were used as received without any further purification.

2.2. Synthesis of MCM-41 and Surface Modification. Mesoporous silicate material MCM-41 was synthesized by the following method (20). A sodium silicate solution was prepared by mixing 7.2 g of fumed silica with 1.3 g of NaOH in doubly distilled water. The resulting solution was heated and stirred at 80 °C for 2 h. The template solution consisted of 7.3 g of cetyltrimethylammonium bromide (CTABr), and 0.7 g of a NH_3 solution (28 %) was dissolved in doubly distilled water followed by heating and stirring for 1 h. Later, the template solution was added simultaneously into a sodium silicate solution with vigorous shaking for 5 min. The resulting gel was then aged overnight at 97 °C. The pH of the gel was adjusted to 10 by the addition of acetic acid before aging again for another 48 h. The final gel molar composition was 6:1.5:0.15:250 SiO_2/CTABr/Na_2O/$(NH_4)_2O$/H_2O. The precipitate of as-synthesized MCM-41 was then filtered, washed with doubly distilled water, and dried overnight in an oven at 97 °C. The final step involved the calcination of an as-synthesized sample at 550 °C to remove the organic template. The calcination temperature was increased from room temperature to 550 °C for 6 h and maintained at that temperature for another 10 h to obtain the final product of MCM-41.

Surface modification of mesoporous silicate material MCM-41 was carried out as follows (22): 1.0 g of a dried MCM-41 powder was mixed with 75 mL of 1,4-butanediol (Aldrich Chemicals) under reflux conditions with a N_2 flow at 230 °C for 24 h. The esterified product (BMCM-41) was filtered, washed with acetone twice, and dried in vacuo.

2.3. Preparation of a BMCM-41/P3HT/Chl Nanocomposite. The nanocomposite of BMCM-41/P3HT/Chl was prepared by the solution-casting method. Typically, 9 mg of a dried BMCM-41 powder was first dispersed in 50 mL of chloroform by sonication in an ultrasonic bath for 30 min to give a stable dispersion solution without aggregation. Then, 1 mg of P3HT was added to the BMCM-41 dispersion solution, and the resulting solution was stirred for 3 h. The resulting solution was added to 100 mL of methanol. Excess solvent was removed by a rotary evaporator to give a BMCM-41/P3HT-10 dispersion in methanol; the number on the right-hand side indicates the polymer percentage (wt %). The remaining methanol was evaporated by a hot plate to obtain the dried powder product. Later, 1 mL of Chl dissolved in benzene (0.5 mg mL^{-1}) was added to 20 mg of a BMCM-41/P3HT-10 conjugate. The absorption equilibrium between Chl and the BMCM-41/P3HT-10 conjugate was established by shaking the suspension in a bioshaker for 1 h at 25 °C. The BMCM-41/P3HT-10/Chl conjugate thus prepared was obtained by centrifugation and dried in vacuo. A similar procedure was used to prepare nanocomposites with 30, 60, and 90 wt % of polymer content.

2.4. Preparation of Photovoltaic Cells. The entire series of photovoltaic cells was prepared in air on glass/ITO substrates. The substrates were cleaned in an ultrasonic bath with acetone and 2-propanol. They were dried and exposed to vacuum ultraviolet-ray (VUV, $\lambda = 172$ nm) for 5 min under reduced pressure (30 Pa). PEDOT—PSS was spin-cast onto the substrate for 30 min at 6000 rpm and dried. The freshly prepared BMCM-41/P3HT/Chl nanocomposites in chloroform (2 mg mL^{-1}) were deposited in air by spin-casting at 2000 rpm for 20 min. The resulting active layer is 200 nm thick. Then, an Al electrode was deposited by evaporation. The active surface is 1 cm².

2.5. Measurements. The FT-IR spectra were recorded on a Spectrum One FT-IR spectrophotometer (Perkin-Elmer, Inc.)

using a KBr disk technique. For IR spectra, 64 scans were collected with a resolution of 0.5 cm^{-1}. Absorption spectra were recorded on a Shimadzu spectrophotometer UV-3600. Nitrogen adsorption−desorption isotherms were recorded by a Belsorp 18Plus-SP instrument (Japan Bell Inc.) at 77 K in the relative pressure range from 0.1 to 0.99. The Brunauer−Emmett−Teller (BET) surface areas were obtained from data under relative pressures between 0.05 and 0.25 before capillary condensation. The pore volumes were determined by a t-plot method. Micro-structural observation was conducted on a Keyence VE 7800 Real Surface View scanning electron microscope (Keyence Corp. Japan) operating at a low voltage of 1 kV to avoid electron charging. Transmission electron microscopy (TEM) images were obtained with a Hitachi H-7500 transmission electron micro-scope using an acceleration voltage of 100 kV. The wide-angle X-ray diffraction (WAXD) measurements were carried out at room temperature on a large Debye−Scherrer camera at the BL02B2 beamline of SPring-8. The incident beam from the bending magnet was monochromatized to $\lambda = 0.100$ nm. The powder samples were packed into glass capillary tubes with an outer diameter of 0.9 mm, and the tubes were rotated during the measurements. The data were collected in a 2θ range from 1 to 75° with a step interval of 0.01°. The scattering vector, q, in specular reflectivity is defined by $q = (4\pi/\lambda) \sin \theta$, where λ and θ are the wavelength and incident angle of the X-ray beam from the horizontal position, respectively. Current−voltage (I−V) curves were performed in air at room temperature by an Agilent E5272A source monitor unit. I−V curves were plotted by Metrics IC/V software. A 300 W xenon arc lamp MAX-302 from Asahi Spectra was used as the light source. The light passes through a CMS-100 monochromator to select 450 nm wave-length. The 450 nm light power was recorded using an Ophir Nova power meter.

3. RESULTS AND DISCUSSION

3.1. Stability of Chl in MCM-41 and BMCM-41.

The adsorption of Chl by a mesoporous material was carried out to test the stability of Chl in MCM-41 and esterified BMCM-41 (23). The products were denoted as MCM-41/Chl and BCMCM-41/Chl. UV−vis absorption spectra of Chl and Chl adsorbed on MCM-41 and BMCM-41 are shown in Figure 1a. The peaks at around 415 and 665 nm are assigned as a Soret band and Q_y transition, respectively. The peaks at 513 and 541 nm are attributed to adsorption of pheophytin (24). In general, the Soret/Q_y ratio of Chl and pheophytin in organic solvents were known to be 1.1−1.3 and 2.2−2.9, respectively (24). The Soret/Q_y ratios of Chl absorbed on MCM-41 and BMCM-41 were 2.2 and 1.3, respectively, indicating that Chl adsorbed on the acidic surface of MCM-41 changed to pheophytin by a loss of centered magnesium ions (Scheme 1). A low Soret/Q_y ratio of Chl during adsorption in BMCM-41 shows that pheophy-tinization was suppressed by the organic group formed by esterification by 1,4-butanediol. Chl pigments adsorbed on pristine MCM-41 and esterified BMCM-41 were extracted with methanol. The spectrum for Chl extracted from BMCM-41 was similar to that for Chl from toluene, suggesting that the Chl molecules in BMCM-41 was quite stable even after 1 month of adsorption, as shown in Figure 1b. The peak observed in BMCM-41/Chl was broader than those observed in monomeric Chl in toluene, which may be explained by the formation of Chl aggregates. On the other hand, decom-position of Chl was observed in the MCM-41/Chl conjugate
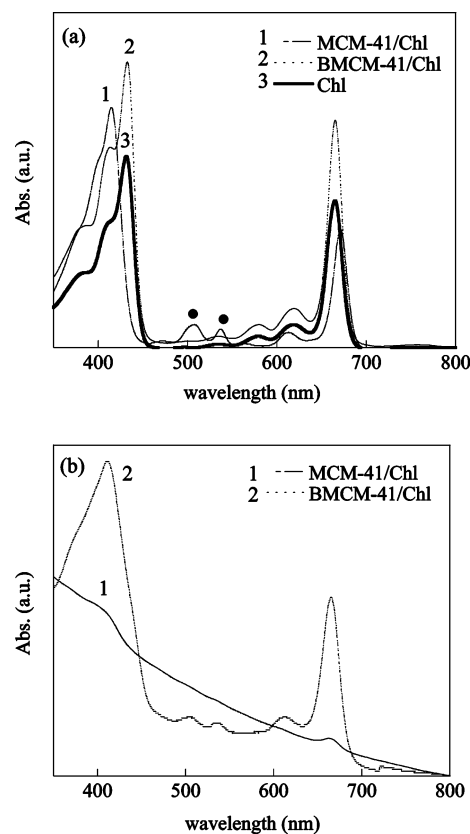

FIGURE 1. (a) UV−vis absorption spectra of Chl and Chl adsorbed on unmodified MCM-41 and esterified BMCM-41. Filled circles denote typical absorption bands of pheophytin. (b) Spectra of Chl adsorbed in MCM-41 and BMCM-41 after 1 month.

as the intensity of a typical Chl absorption at Soret and Q_y bands decreased significantly. This result demonstrates the importance of using esterified BMCM-41 as a better host for stable Chl adsorption compared to MCM-41.

3.2. WAXD Measurement and TEM Observa-tion.

Figure 2 shows the WAXD patterns of MCM-41, esterified BMCM-41, P3HT, and BMCM-41/P3HT nanocom-posites at different P3HT contents. The Bragg peak of the MCM-41 diffractogram (Figure 2a) can be indexed as hkl reflections of a regular hexagonal array of uniform channels with an interplanar spacing of 3.85 nm. The observations of one sharp peak at $q = 1.63$ nm^{-1} with two weaker peaks at $q = 2.74$ and 3.17 nm^{-1} were assigned to (100), (110), and (200) reflections of the hexagonal structure, which is a typical characteristic of MCM-41 (25). It can be seen from the diffractogram (Figure 2b) that the esterified BMCM-41 (100) peak shifted to a lower q value compared to that of pristine MCM-41. The shifting might be caused by the increased distance between planes after grafting of the butanol group onto the silica surface. Similar trends were reported on other organically modified silica materials (21, 26, 27). It is clear that P3HT exhibits an interchain lamellar structure with a lamellar distance estimated from the P3HT diffractogram (Figure 2g) of 1.64 nm (28). This interchain lamellar structure arises from the packing of P3HT hexyl group side chains, as shown in Scheme 2. The mor-phology of the nanocomposites can be determined by monitoring the position, shape, and intensity of the reflec-

 Yah et al.

Scheme 1. Schematic Model for the Adsorption of Chl Molecules on the Surface of Unmodified MCM-41 and Esterified BMCM-41
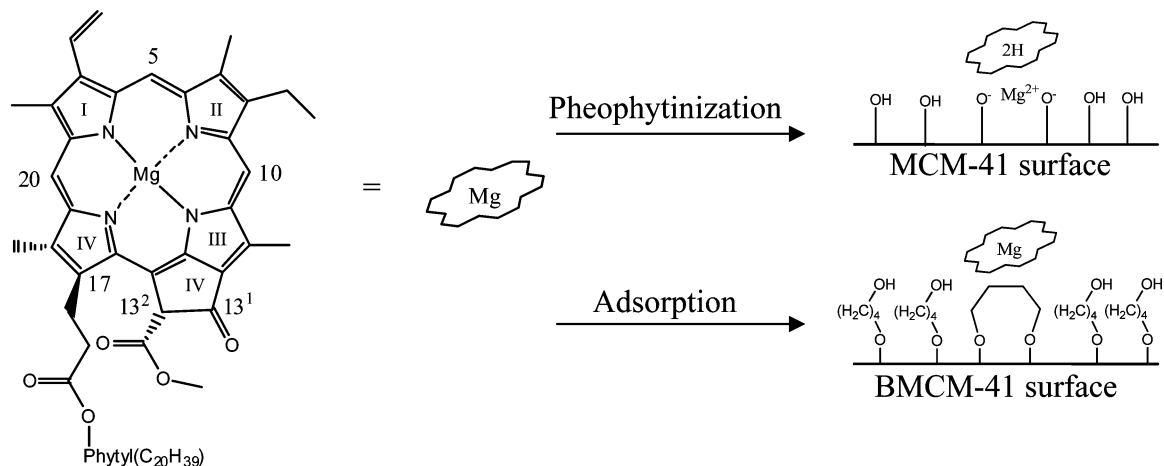
tions from the WAXD pattern. For instance, in the case of a layered silicate material, if the coherent diffraction from the silicate layer eventually disappeared caused by extensive layer separation associated with the delamination of the silicate layer in the polymer matrix, it could be classified as
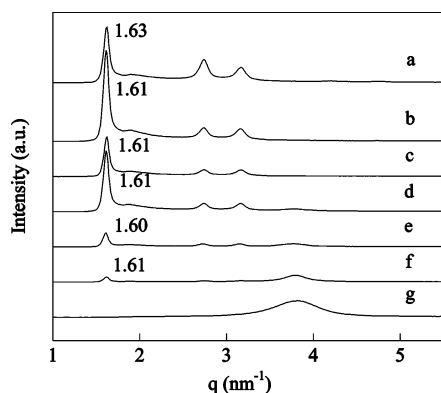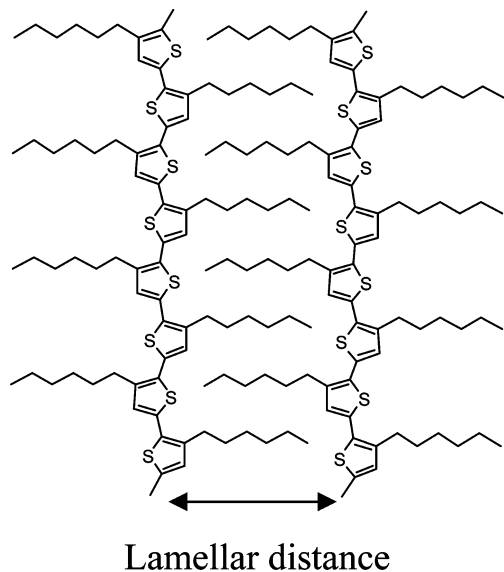
Table 1. Interplanar Spacing of MCM-41 and the Lamellar Thickness of P3HT in Nanocomposites

sample	MCM-41 interplanar spacing, d_{100} (nm)	P3HT lamellar distance (nm)
MCM-41	3.85	
BMCM-41	3.90	
BMCM-41/P3HT-10	3.90	unrecognizable
BMCM-41/P3HT-30	3.90	1.67
BMCM-41/P3HT-60	3.93	1.67
BMCM-41/P3HT-90	3.90	1.65
P3HT		1.64

an exfoliated nanocomposite. In contrast, if the layer expansion associated with polymer intercalation results in the appearance of a new intrinsic reflection corresponding to the larger interplanar spacing, then it would be labeled as an intercalated nanocomposite (29). The interplanar spacing of MCM-41 and lamellar thickness of P3HT in nanocomposites are presented in Table 1. The diffractograms (Figure 2c−f) for BMCM-41/P3HT nanocomposites with different P3HT concentrations (10, 30, 60, and 90 wt %) exhibit a shifting of the P3HT lamellar peak to a lower q value ($q = 3.77$ nm^{-1}), i.e., giving an increase in the interchain lamellar distance by 0.03 nm. The hexagonal peaks of BMCM-41 become broader with lower intensity when the P3HT content was increased from 10 to 90 wt %. The expansion of the P3HT lamellar coupled with a reduction of the BMCM-41 hexagonal crystallinity implies that the atomic arrangement of the silicate mesophase wall becomes disordered upon intercalation of P3HT lamella. Nevertheless, it is obvious that the peak positions of BMCM-41/P3HT nanocomposites are identical with those of pure P3HT and MCM-41, indicating that both MCM-41 and P3HT unit cell structures remain unaffected in nanocomposites even after surface modification and P3HT chain intercalation.

The macroscopic feature of this MCM-41/P3HT conjugate was further elucidated by TEM. TEM micrographs of selected BMCM-41/P3HT with 10, 30, 60, and 90 wt % of the P3HT content are shown in Figure 3. It was observed that even after MCM-41 underwent surface modification with 1,4-butanediol and was mixed with P3HT via a solution-casting

FIGURE 2. WAXD patterns of MCM-41/P3HT nanocomposites: (a) MCM-41; (b) BMCM-41; (c) BMCM-41/P3HT-10; (d) BMCM-41/P3HT-30; (e) BMCM-41/P3HT60; (f) BMCM-41/P3HT-90; (g) P3HT.

Scheme 2. Schematic Model of Lamellar P3HT
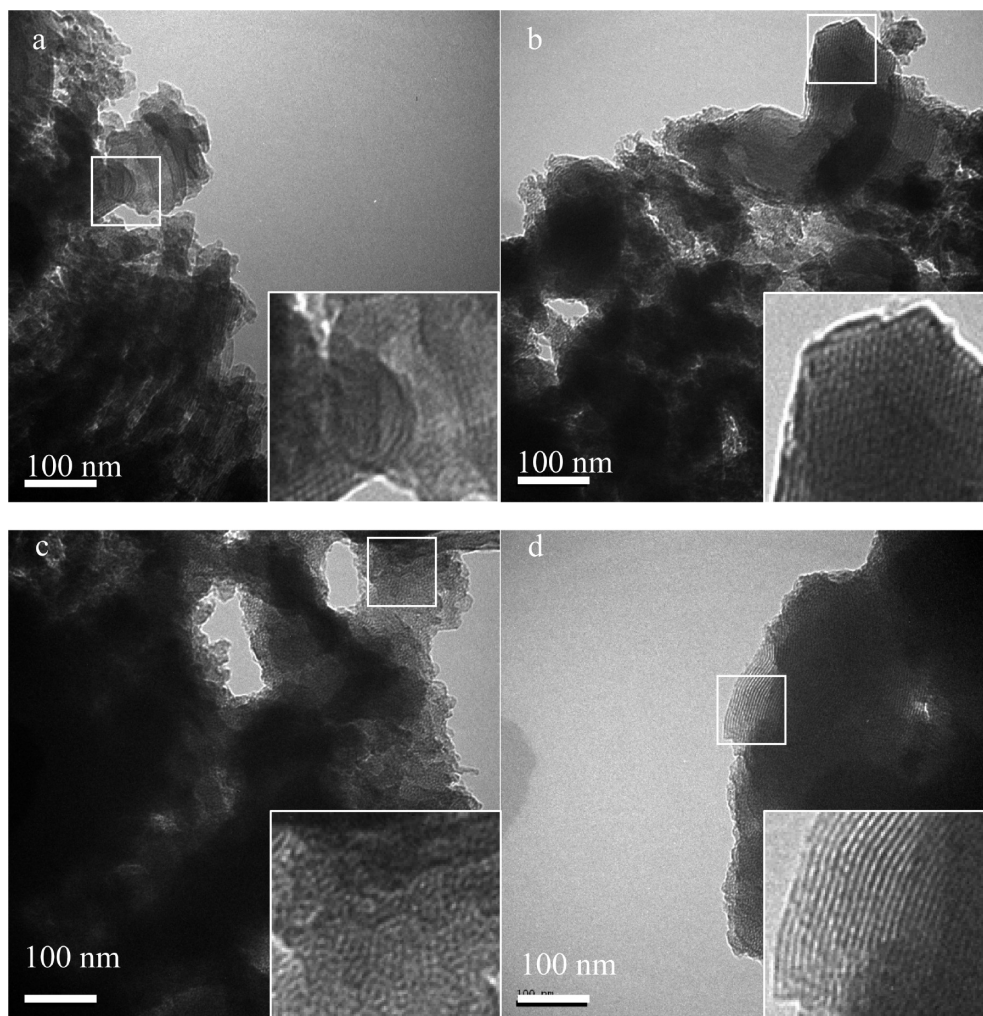

Lamellar distance

FIGURE 3. TEM micrographs of BMCM-41/P3HT nanocomposites: (a) BMCM-41/P3HT-10; (b) BMCM-41/P3HT-30; (c) BMCM-41/P3HT-60; (d) BMCM-41/P3HT-90. Insets: 3× enlargements of the indicated areas.

method, an ordered array of the MCM-41 pore structure was still retained. Nevertheless, some areas of the samples were not highly ordered probably because of the collapse of the pore structure during the hybridization process with P3HT via a solution-casting method. The pore size of MCM-41 could be roughly estimated to be ca. 3 nm. However, the hexagonal pore structure of the sample is hardly recognizable because of the low resolution of the micrograph. The micrograph shows that not all of the BMCM-41 pore was blocked by an intercalated P3HT chain. These open spaces will be ideal sites for further Chl immobilization.

3.3. Scanning Electron Microscopy (SEM).
The structure of the BMCM-41/P3HT/Chl film on silicon substrates was observed by SEM. Figure 4 shows SEM images for the film of MCM-41/P3HT-n/Chl with n = polymer content of (a) 10 wt %, (b) 30 wt %, (c) 60 wt %, and (d) 90 wt %. All samples were obtained by spin-coating from a chloroform solution. Figure 4a shows that BMCM-41 nanoparticles act as fillers and are embedded in the P3HT matrix. It is clearly observed that the BMCM-41 nanoparticles are dispersed homogeneously and possess higher surface areas in contact with the P3HT matrix. Nonuniform distribution of BMCM-41 started to appear when the P3HT content was

increased to 30 wt % (Figure 4b). Similar results were observed when the P3HT content was increased to 60 (Figure 4c) and 90 wt % (Figure 4d) because the BMCM-41 dispersion becomes nonuniform, with some of them totally covered with the P3HT polymer matrix.

3.4. Nitrogen Adsorption−Desorption Isotherm.
The nitrogen adsorption−desorption isotherm for MCM-41, surface-modified BMCM-41, and BMCM-41/P3HT nanocomposites are shown in Figure 5. The isotherms of MCM-41 and BMCM-41 are distinctive of irreversible type IV adsorption with two separate H1 and H4 hysterisis loops (30). The MCM-41 isotherm shows that the initial region can be extrapolated back to the origin, confirming the absence of any detectable micropore filling at $p/p_0 < 0.3$. However, the BMCM-41 isotherms show that micropore filling started at $p/p_0 = 0.2$, indicating shrinkage of the MCM-41 pore caused by grafting of the 1,4-butanediol group. This trend is in good agreement with previous results of the mesoporous silica adsorption isotherm before and after surface modification (31, 32). Nitrogen adsorption−desorption isotherms of BMCM-41/P3HT conjugates were done in which various amounts of P3HT (10−90 wt %) were examined. As can be observed from Figure 5, with an increase in the amount of P3HT
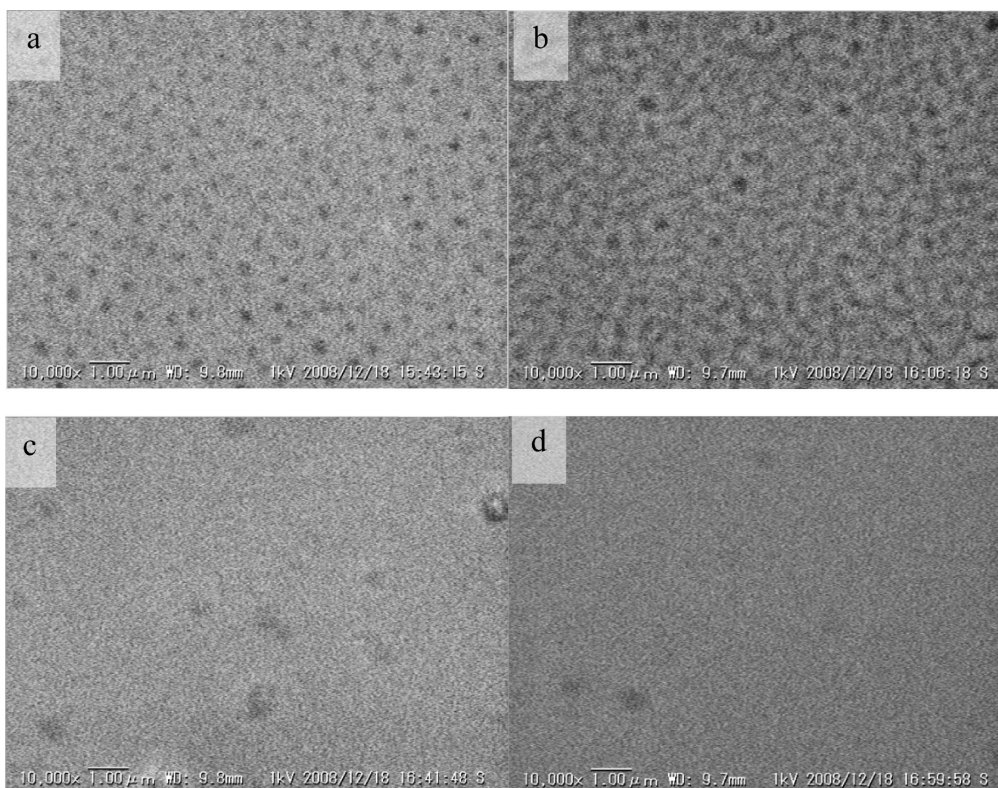
FIGURE 4. SEM top-view images of nanocomposites spin-cast from a chloroform solution: (a) BMCM-41/P3HT-10/Chl; (b) BMCM-41/P3HT-30/Chl; (c) BMCM-41/P3HT-60/Chl; (d) BMCM-41/P3HT-90/Chl.
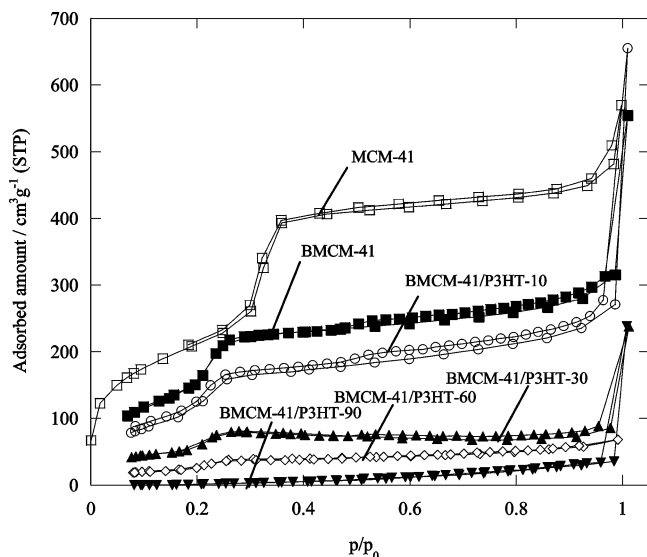

FIGURE 5. Nitrogen adsorption−desorption isotherms of MCM-41 (□), BMCM-41 (■), BMCM-41/P3HT-10 (○), BMCM-41/P3HT-30 (▲), BMCM-41/P3HT-60 (◇), and BMCM-41/P3HT-90 (▼).

Table 2. Pore Characterization of MCM-41, BMCM-41, and Their Nanocomposites

sample	BET surface area (m^2 g^{-1})	pore volume (mL g^{-1})	pore size (nm)
MCM-41	786	0.81	4.1
BMCM-41	584	0.55	3.8
BMCM-41/P3HT-10	590	0.52	3.5
BMCM-41/P3HT-30	270	0.22	3.2
BMCM-41/P3HT-60	140	0.11	3.0
BMCM-41/P3HT-90	nonporous	nonporous	nonporous
BMCM-41/P3HT-10/Chl	596	0.43	2.9
BMCM-41/P3HT-30/Chl	211	0.16	3.1
BMCM-41/P3HT-60/Chl	81	0.05	2.2
BMCM-41/P3HT-90/Chl	nonporous	nonporous	nonporous

of BMCM-41/P3HT/Chl were less than half of that of BMCM-41/P3HT (Table 2). This indicates that Chl was successfully immobilized into the pore BMCM-41/P3HT conjugates.

3.5. UV−Vis Absorption Spectra. The UV−vis absorption spectra of BMCM-41/P3HT/Chl nanocomposites and pure P3HT in chloroform are shown in Figure 6. The pure P3HT exhibits the maximum absorption at 451 nm, which corresponds to the $\pi-\pi^*$ transition of π-conjugated segments of P3HT. By the addition of BMCM-41 nanoparticles from 10 to 60 wt %, the 451 nm peak shows a blue shift to lower wavelength relative to pure P3HT. This blue shift of the $\pi-\pi^*$ transition band due to the reduction of the P3HT-conjugated length arises from different structures of P3HT in the nanocomposites in comparison to the pure P3HT. The maximum blue shift is observed from sample a, with the hump at 665 nm attributed to the Q_y band of Chl

intercalated to the BMCM-41 pore, the amount of nitrogen adsorbed to the BMCM-41/P3HT conjugate decreased. The nitrogen uptake by BMCM-41/P3HT-90 is the lowest in comparison to that of the samples with 10, 30, and 60 wt % P3HT contents. This result coupled with a reduction of the surface area and pore volume indicates that the BMCM-41 pores were filled with P3HT. The BET surface areas and pore volumes of BMCM-41/P3HT conjugates decreased further when Chl was adsorbed to the remaining spaces of BMCM-41/P3HT conjugates. In this case, the pore volumes
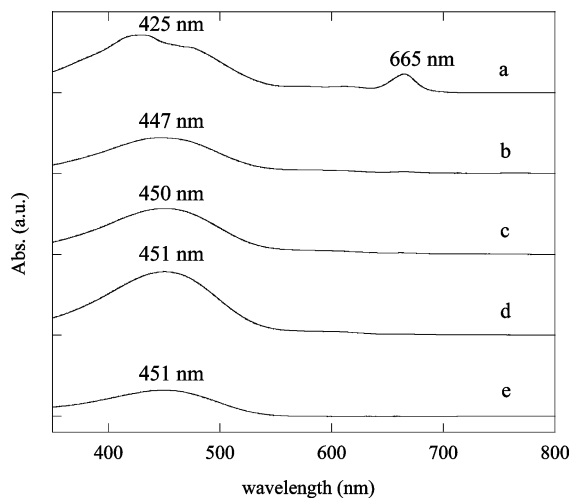
FIGURE 6. UV−vis spectra of (a) BMCM-41/P3HT-10/Chl, (b) BMCM-41/P3HT-30/Chl, (c) BMCM-41/P3HT-60/Chl, (d) BMCM-41/P3HT-90/Chl, and (e) P3HT. Samples b−d were 15 times diluted.

Table 3. Q_y Absorption Intensity and Amount of Chl Absorbed in 1 g of BMCM-41/P3HT-n, Where n = 10, 30, 60, and 90 wt % of P3HT Content

sample	Q_y band absorption	amount of Chl in a 1 g sample (mg)
BMCM-41/P3HT-10/Chl	0.115	5.54
BMCM-41/P3HT-30/Chl	0.096	4.62
BMCM-41/P3HT-60/Chl	0.097	4.69
BMCM-41/P3HT-90/Chl	0.061	2.94

(note that samples b−d were diluted 15 times for better comparison; therefore, the Q_y band is not observable). The further blue shift of the $\pi-\pi^*$ transition band for sample a indicates that the introduction of 90 wt % of BMCM-41 nanoparticles into the P3HT matrix may result in a disordered conformation of polymer chains (21). Interactions might have formed between Chl and P3HT in the mesopore of BMCM-41 in which Chl alters the P3HT conformation, thus shortening the effective conjugation length of P3HT. It may also be proposed that the amount of intercalated P3HT chain inside the mesopore over the bulk P3HT is the highest for sample a that reduces the average P3HT interchain distance, thereby giving the highest blue shift. In contrast, samples b−d have lower intercalated P3HT to bulk P3HT ratios and fewer P3HT chains in compact form. As a result, a decrease in the blue shift is observed from sample b to d. Nevertheless, a similar blue shift was reported in the UV−vis absorption of FeCl₃-doped P3HT (33) and a poly(3HT-co-3TPP)−silica system (34).

The amount of Chl adsorbed in the BMCM-41/P3HT conjugate was calculated from UV−vis absorbance using the molar extinction coefficient of Chl (9.25×10^4 M^{-1} cm^{-1}) at 661.6 nm in acetone (35). The amounts of Chl absorbed in 1 g of BMCM-41/P3HT-n, where n = 10, 30, 60, and 90 wt % of P3HT content, are shown in Table 3. It is obvious that an increase in the amount of P3HT content leads to a decrease in the adsorption of Chl. Because of the highest pore volume of BMCM-41/P3HT-10 compared to other samples as shown in the nitrogen adsorption−desorption result, large amounts of Chl could be adsorbed into the
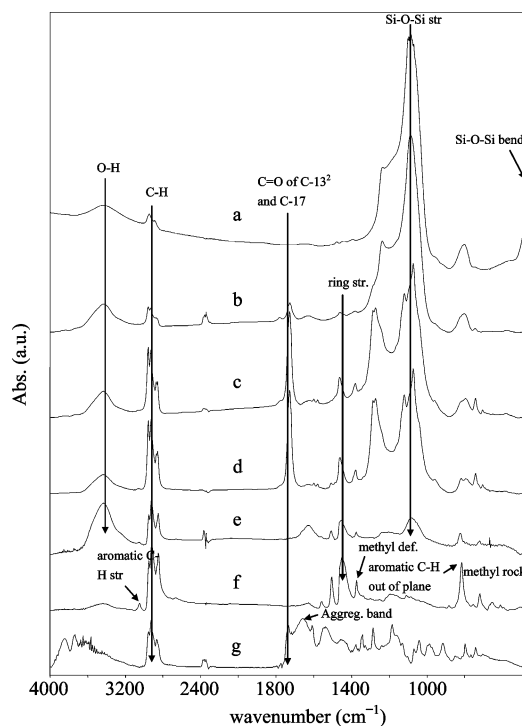

FIGURE 7. FT-IR spectra of nanocomposites: (a) BMCM-41; (b) BMCM-41/P3HT-10/Chl; (c) BMCM-41/P3HT-30/Chl; (d) BMCM-41/P3HT-60/Chl; (e) BMCM-41/P3HT-90/Chl; (f) P3HT; (g) Chl.

remaining spaces of the BCMCM-41/P3HT conjugate. Likewise, the amounts of Chl adsorbed to BMCM-41/P3HT-30 and BMCM-41/P3HT-60 are relatively lower compared to those of BMCM-41/P3HT-10 because of its smaller pore volume and surface area. It is known that OH groups from BMCM-41 play an important role in Chl adsorption because they can form hydrogen bonds between each other (22). Increasing the amount of the P3HT content will hinder the free access of Chl to the BMCM-41 surface. Consequently, less Chl was adsorbed stably inside the pore and free Chl was removed during solution casting. However, the BMCM-41/P3HT-90 conjugate that exhibits nonporous properties was able to absorb half the amount of Chl as BMCM-41/P3HT-10. This was ascribed to the absorption of free Chl molecules that attached to the bulk P3HT, which was not immobilized inside the BMCM-41 mesopore.

3.6. FT-IR Spectra. The FT-IR spectra for Chl, P3HT, and BMCM-41/P3HT/Chl nanocomposites are presented in Figure 7. For Chl, the bands at 2870−2970 cm^{-1} are for the aliphatic C−H stretching of the phytyl group and alkyl groups on the porphyrin ring. The band at 1738 cm^{-1} is assigned to the two ester groups of C-13 and C-17 (Scheme 1). The aggregation band of Chl at 1657 cm^{-1} is also present (36). For P3HT, there are absorption bands at 2954, 2923, and 2853 cm^{-1} for aliphatic C−H stretching, 1508 and 1454 cm^{-1} for ring stretching, 1377 cm^{-1} for methyl deformation, 820 cm^{-1} for aromatic C−H out of the plane, and 724 cm^{-1} for methyl rocking (37). For BMCM-41, the O−H absorption bands at 3435 cm^{-1} and aliphatic C−H stretching bands at 2949 and 2890 cm^{-1} are due to the hydroxybutyl groups of modified MCM-41. The silicate-related bands are 1088 cm^{-1} for Si−O−Si stretching with a shoulder at 1236 cm^{-1} and
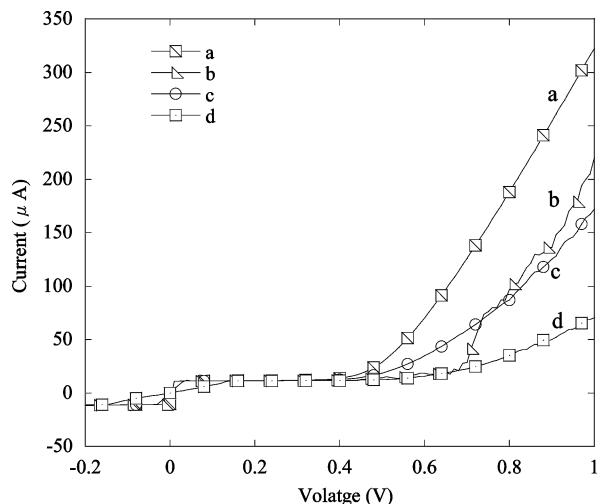
FIGURE 8. *I*−*V* characteristics of nanocomposites: (a) BMCM-41/P3HT-10/Chl; (b) BMCM-41/P3HT-30/Chl; (c) BMCM-41/P3HT-60/Chl; (d) BMCM-41/P3HT-90/Chl.

Table 4. Photovoltaic Parameters of BMCM-41/PHT/Chl Devices for Different P3HT Contents

parameter	BMCM-41/P3HT-10/Chl	BMCM-41/P3HT-30/Chl	BMCM-41/P3HT-60/Chl	BMCM-41/P3HT-90/Chl
I_{SC} (μA)	10.40	1.10	0.95	0.01
V_{OC} (mV)	4.80	0.80	0.72	0.21
FF	0.29	0.29	0.23	0.27
IPCE$_{450}$ (%)	7.16	0.76	0.65	0.01

463 cm^{-1} for Si−O−Si bending (38). The distinctive absorption bands of BMCM-41, P3HT, and Chl in nanocomposites are retained. At high BMCM-41 concentration, the intensity of the silicate peaks is higher; likewise, when the silica content is reduced, the intensity of the corresponding peaks becomes lower. It has been noticed from the FT-IR data that the Si−O−Si frequency of BMCM-41 at 1088 cm^{-1} is the same as that for BMCM-41/P3HT-10/Chl, while it decreased to 1074 cm^{-1} for both BMCM-41/P3HT-30/Chl and BMCM-41/P3HT-60/Chl and to 1083 cm^{-1} for BMCM-41/P3HT-90/Chl. The shift in the Si−O−Si vibration frequency for BMCM-41/P3HT-30,60,90/Chl may be due to the intercalation of P3HT lamella into the mesopore of BMCM-41, which hinders Si−O−Si from vibrating freely, thus shifting the Si−O−Si frequency to a lower value. The same explanation follows for the P3HT ring stretching at 1454 cm^{-1}, which increased to 1463 cm^{-1} for BMCM-41/P3HT-10/Chl, 1464 cm^{-1} for both BMCM-41/P3HT-30/Chl and BMCM-41/P3HT-60/Chl, and 1457 cm^{-1} for BMCM-41/P3HT-90/Chl. This is because intercalation of P3HT lamella into the BMCM-41 mesopore makes the P3HT lamella more compact, shifting the P3HT ring absorption to a higher frequency value. Nevertheless, except for BMCM-41/P3HT-90/Chl, the ester group that absorbs at 1738 cm^{-1} shifted to 1728 cm^{-1} for BMCM-41/P3HT-10/Chl and 1729 cm^{-1} for both BMCM-41/P3HT-30/Chl and BMCM-41/PHT-60/Chl. The shifting to a lower frequency may be due to the formation of hydrogen bonds between Chl ester groups and OH groups of BMCM-41.

3.7. *I*−*V* Measurements. *I*−*V* characteristics of BMCM-41/P3HT/Chl with different polymer contents are shown in Figure 8. Monochromatic light of 450 nm with a power of 0.4 mW cm^{-2} was irradiated from the ITO side. We have measured the short-circuit current (I_{SC}), open-circuit voltage (V_{OC}), fill factor (FF), and incident photon-to-current conversion efficiency (IPCE) from the *I*−*V* curves. The photovoltaic parameters are summarized in Table 4. In this system, electrons generated by an electron donor of P3HT will be transferred to an electron acceptor of Chl (HOMO and LUMO levels of P3HT were 4.9 and 2.8 eV, respectively, while those

of Chl were 4.9 and 3.24 eV, respectively) (39). It was reported that simple blending of P3HT and Chl failed to generate photoinduced electrons because of an improper inner cell driving force (39−41). Interestingly, a photoinduced carrier is observed when MCM-41 mesoporous nanoparticles were added to the P3HT/Chl system. The improvement of the photovoltaic properties upon the addition of MCM-41 into the P3HT/Chl system can be explained by several phenomena: (i) Semiconductivity of MCM-41. It was reported that surface states present on the internal surfaces of the MCM-41 mesopore can overlap to generate energy bands, granting this silica material semiconducting properties (42). It might be this semiconducting MCM-41 that improved the photovoltaic properties of the P3HT/Chl blend system. (ii) Enlargement of the interfacial contact area. As has been discussed in the nitrogen adsorption−desorption results, MCM-41 exhibits a high surface area of 786 m^2 g^{-1} and can provide a larger contact area for this blend system, resulting in more efficient charge separation between P3HT and Chl. (iii) Efficient exciton diffusion in the MCM-41 mesopore. The exciton diffusion lengths in the conducting polymer and dye are typically 10 nm. Because both P3HT and Chl were immobilized inside a mesopore of 4 nm, which falls within the range of the diffusion length, efficient photoexcited exciton diffusion to a dissociation site could be achieved (43).

Enhancement of the photovoltaic properties is observed when the P3HT content was decreased from 90 to 10 wt %, with larger increases in the photocurrent and open circuit voltage obtained for the sample of 10 wt % P3HT content. The photovoltaic performance improvement upon a reduction in the nanocomposite P3HT amount from 90 to 10 wt % is shown by the increase of IPCE from 0.01 to 7.16%. It seems that not only MCM-41 will affect the photovoltaic properties in this system, but the concentration of Chl immobilized inside the pore will also play an important role in the enhancement of the photovoltaic effect. As can be reviewed in the UV−vis results, BMCM-41/P3HT-10/Chl apparently has a higher concentration of immobilized Chl. This photosynthetic dye contributes a synergy effect of increasing the conductivity of the active organic layer via doping as well as improving the light-harvesting capability for an enhanced photovoltaic efficiency. There is a possibility that the photovoltaic property of this nanocomposite could be further improved if the P3HT content is less than 10 wt %. Nevertheless, more experiments will be conducted in order to clarify this point.

4. CONCLUSIONS

Surface-modified MCM-41 produces nanocomposites with P3HT and Chl by casting from chloroform. 1,4-Butanediol-modified BMCM-41 is critical for stable adsorption of Chl. The pore structure of BMCM-41 was retained after intercalation of P3HT, as evidenced from WAXD and TEM studies. A decrease in the d_{100} peak intensity of P3HT from WAXD results, coupled with a reduction in the pore volume and surface area of BMCM-41, confirmed that intercalation of P3HT chains inside the mesopore was successfully carried out. SEM observations show more a homogeneous distribution of BMCM-41 nanoparticles in a BMCM-41/P3HT-10/Chl polymer matrix. The UV−vis study shows a blue shift in the spectra of BMCM-41/P3HT/Chl nanocomposites. The FT-IR study indicates an increase in the thiophene ring stretching frequency for a P3HT intercalated structure and a decrease in the C═O stretching frequency for immobilized Chl ester groups. The photovoltaic property of Chl-doped P3HT was enhanced significantly upon the addition of BMCM-41. The highest IPCE of BMCM-41/P3HT-10/Chl is 7.16% in these nanocomposites.

Note Added after ASAP Publication. This article was published ASAP on July 2, 2009, with incorrect affiliations. The correct version was published on July 7, 2009.

REFERENCES AND NOTES

(1) Kido, J.; Shionoya, H.; Nagai, K. *Appl. Phys. Lett.* **1995**, *67*, 2281–2283.

(2) Ohmori, Y.; Hironaka, Y.; Yoshida, R.; Fujii, A.; Tada, N.; Yoshino, K. *Polym. Adv. Technol.* **1997**, *8*, 403–407.

(3) Cabanillas-Gonzalez, J.; Yeates, S.; Bradley, D. D. C. *Synth. Met.* **2003**, *139*, 637–641.

(4) Tanigaki, N.; Mochizuki, H.; Mo, X.; Mizokuro, T.; Hiraga, T.; Taima, T.; Yase, K. *Thin Solid Films* **2006**, *499*, 110–113.

(5) Sicot, L.; Fiorini, C.; Lorin, A.; Nunzi, J. M.; Raimond, P.; Sentein, C. *Synth. Met.* **1999**, *102*, 991–992.

(6) Aihara, S.; Hirano, Y.; Tajima, T.; Tanioka, K.; Abe, M.; Saito, N. *Appl. Phys. Lett.* **2003**, *82*, 511–513.

(7) Fuller, M. J.; Walsh, C. J.; Zhao, Y.; Wasielewski, M. R. *Chem. Mater.* **2002**, *14*, 952–953.

(8) Yoshino, K.; Tada, K.; Hirohata, M.; Kajii, H.; Hironaka, Y.; Tada, N.; Kaneuchi, Y.; Yoshida, M.; Fujii, A.; Kawai, T.; Araki, H.; Ozaki, M.; Ohmori, Y.; Onoda, M.; Zakhidov, A. A.; Hamaguchi, M. *Synth. Met.* **1997**, *84*, 477–482.

(9) Ltaief, A.; Ben-Chadbane, R.; Bouazizi, A.; Davenas, J. *Mater. Sci. Eng., C* **2006**, *26*, 344–347.

(10) Heffner, G. W.; Pearson, D. S. *Macromolecules* **1991**, *24*, 6295–6299.

(11) Takahashi, K.; Iwanaga, T.; Yamaguchi, T.; Komura, T.; Murata, K. *Synth. Met.* **2001**, *123*, 91–94.

(12) Imoto, K.; Takahashi, K.; Yamaguchi, T.; Komura, T.; Nakamura, J. I.; Murata, K. *Bull. Chem. Soc. Jpn.* **2003**, *76*, 2277–2283.

(13) Krebs, F. C.; Biancardo, M. *Sol. Energy Mater. Sol. Cells* **2006**, *90*, 142–165.

(14) Fleming, I. *Nature* **1967**, *216*, 151–152.

(15) Norris, R.; Uphaus, R. A.; Crespi, H. L.; Katz, J. J. *Proc. Natl. Acad. Sci. U.S.A.* **1971**, *68*, 625–628.

(16) Inamura, I.; Ochiai, H.; Toki, K.; Ishine, Y.; Araki, T. *Chem. Lett.* **1985**, *14*, 381–384.

(17) Radwan, R. M.; Lotfy, S.; Desouky, O. S. *Nucl. Instrum. Methods Phys. Res., Sect. B* **2008**, *266*, 3953–3958.

(18) Itoh, T.; Asada, H.; Tobioka, K.; Kodera, Y.; Matsushima, A.; Hiroto, M.; Nishimura, H.; Kamachi, T.; Okura, I.; Inada, Y. *Bioconjugate Chem.* **2000**, *11*, 8–13.

(19) Kodera, Y.; Kageyama, H.; Sekine, H.; Inada, Y. *Biotechnol. Lett.* **1992**, *14*, 119–122.

(20) Kresge, C. T.; Leonowicz, M. E.; Roth, W. J.; Vartuli, J. C.; Beck, J. S. *Nature* **1992**, *359*, 710–712.

(21) Kuila, B. K.; Nandi, A. K. *Macromolecules* **2004**, *37*, 8577–8584.

(22) Murata, S.; Hata, M.; Kimura, T.; Sugahara, Y.; Kuroda, K. *Langmuir* **2000**, *16*, 7106–7108.

(23) Murata, S.; Furukawa, H.; Kuroda, K. *Chem. Mater.* **2001**, *13*, 2722–2729.

(24) Perkins, H. J.; Roberts, D. W. A. *Biochim. Biophys. Acta* **1964**, *79*, 20–29.

(25) Beck, S.; Vartuli, J. C.; Roth, W. J.; Leonowicz, M. E.; Kresge, C. T.; Schmitt, K. D.; Chu, C. T. W.; Olson, D. H.; Sheppard, E. W.; McCullen, S. B.; Higgins, J. B.; Schlenker, J. L. *J. Am. Chem. Soc.* **1992**, *114*, 10834–10843.

(26) Ray, S. S.; Maiti, P.; Okamoto, M.; Yamada, K.; Ueda, K. *Macromolecules* **2002**, *35*, 3104–3110.

(27) Maiti, P.; Yamada, K.; Okamoto, M.; Ueda, K.; Okamoto, K. *Chem. Mater.* **2002**, *14*, 4654.

(28) Pal, S.; Nandi, A. K. *Macromolecules* **2003**, *36*, 8426–8432.

(29) Ray, S. S.; Okamoto, M. *Prog. Polym. Sci.* **2003**, *28*, 1539–1641.

(30) Koopar, K. In *Manual of Symbol and Terminology for Physicochemical Quantities and Units: Appendix II: Definitions Terminology and Symbols in Colloid and Surface Chemistry*,; Everett, D. H., Ed.; IUPAC Council: Washington, DC, 2001; p 12.

(31) Inagaki, S.; Koiwai, A.; Suzuki, N.; Fukushima, Y.; Kuroda, K. *Bull. Chem. Soc. Jpn.* **1996**, *69*, 1449–1457.

(32) Kimura, T.; Kuroda, K.; Sugahara, Y.; Kuroda, K. *J. Porous Mater.* **1998**, *5*, 127–132.

(33) Singh, R. K.; Kumar, J.; Singh, R.; Kant, R.; Chand, S.; Kumar, V. *Mater. Chem. Phys.* **2007**, *104*, 390–396.

(34) Yu, Y.; Lai, C.; Chen, C.; Yeh, J. *J. Electron. Mater.* **2006**, *35*, 1571–1580.

(35) Lichtenthaler, H. K. *Methods Enzymol.* **1987**, *148*, 350–382.

(36) Anderson, F. H.; Calvin, M. *Arch. Biochem. Biophys.* **1964**, *107*, 251–259.

(37) Chen, T.; Wu, X.; Rieke, R. D. *J. Am. Chem. Soc.* **1995**, *117*, 233–244.

(38) Zhao, X. S.; Lu, G. Q.; Millar, G. J. *Ind. Eng. Chem. Res.* **1996**, *35*, 2075–2090.

(39) Jenekhe, S. A.; Vaithianathan, V.; Yun, J.; Jung, H.; Kim, S.; Han, E. *Appl. Phys. Lett.* **2005**, *87*, 123102.

(40) Parker, D. *J. Appl. Phys.* **1994**, *75*, 1656–1666.

(41) Brabec, C. J.; Cravino, A.; Meissner, D.; Sariciftci, N. S.; Fromherz, T.; Rispens, M. T.; Sanchez, L.; Hummelen, J. C. *Adv. Funct. Mater.* **2001**, *11*, 374–380.

(42) Cai, Q.; Zou, W. Y.; Luo, Z. S.; Wen, Q. X.; Pang, W. Q.; Cui, F. Z. *Mater. Lett.* **2003**, *58*, 1–4.

(43) Halls, J. J. M.; Pichler, K.; Friend, R. H.; Moratti, S. C.; Holmes, A. B. *Appl. Phys. Lett.* **1996**, *68*, 3120–3122.

AM9002099